International Journal of Fatigue 160 (2022) 106862

Contents lists available at ScienceDirect

International Journal of Fatigue

journal homepage: www.elsevier.com/locate/ijfatigue

Interior initiation and early growth of very high cycle fatigue crack in an additively manufactured Ti-alloy

Weiqian Chi [a,b], Gen Li [b], Wenjing Wang [a,*], Chengqi Sun [b,c,*]

[a] Key Laboratory of Vehicle Advanced Manufacturing, Measuring and Control Technology (Beijing Jiaotong University), Ministry of Education, Beijing, 100044, China
[b] State Key Laboratory of Nonlinear Mechanics, Institute of Mechanics, Chinese Academy of Sciences, Beijing 100190, China
[c] School of Engineering Science, University of Chinese Academy of Sciences, Beijing 100049, China

ARTICLE INFO

Keywords:
Additively manufactured titanium alloy
Very high cycle fatigue
Interior crack initiation
Ultralow crack growth rate
Grain refinement

ABSTRACT

Very high cycle fatigue of an additively manufactured Ti-6Al-4V is studied at R = -1, 0.1 and 0.2. The fracture surface of crack initiation and early growth region presents fine granular area (FGA) morphology with discontinuous regions of nanograins. The equivalent crack growth rate in FGA is in the magnitude of 10^{-13}-10^{-11} m/cyc based on the "tree ring" patterns marked on fracture surface. Interior crack initiation and early growth is attributed to the cracks caused by nanograins formed during fatigue loading and the cracks formed irrespective of nanograins. The crack growth rate in FGA is also used to predict the fatigue life.

1. Introduction

Additively manufactured (AM) titanium alloys, due to the shorter production cycle of AM technique in small lot sizes or component parts with complicated geometries, have potential use in aerospace, biomedical and nuclear industries [1–4], in which some of the components suffer from fatigue loadings in service. Similar to the traditionally manufactured metallic materials (e.g. titanium alloys [5–7], steels [8–12], aluminum alloys [13–15], Ni-based single crystal superalloys [16]), the AM titanium alloys [17–19] could still fail at the fatigue cycles bigger than 10^7 at which the traditional fatigue limit is defined. The study for the fatigue behavior beyond 10^7 loading cycles, i.e. very high cycle fatigue (VHCF), has become a new field of fatigue research for the demand of ultralong fatigue life of components in service.

Fatigue crack in VHCF often initiates from the interior of the specimen, and the fracture surface presents fine granular area (FGA) (also called "dark area" [20], "granular bright facet" [21]) or rough area (RA) in the crack initiation and early growth region for high strength steels and titanium alloys. Many studies have shown that the FGA or RA consumes most of the fatigue life in VHCF regime [8–10,22,23], and the microstructure in FGA or RA presents a thin layer of refined grains [24–26], no refined grain feature [23,27,28], or discontinuous regions of refined grains [11,29,30]. Hence, a fully understanding of FGA or RA formation is crucial for elucidating the mechanism of crack initiation and early growth in VHCF regime. Different models have been developed for FGA formation [9,31,32], such as "hydrogen assisted crack growth" model [8], "polygonization and micro-debonding" model [27], and "numerous cyclic pressing" model [28]. Among these models, one popular viewpoint is that the FGA is formed after the fatigue crack formation and is related to the repeated contact of fracture surfaces [28,32,33]. While another popular viewpoint is that FGA is formed before the fatigue crack formation and is related to the grain refinement caused by dislocation interaction [24,29,34,35]. Therefore, the formation of FGA or RA needs to be further elucidated in VHCF regime.

Differing from the conventionally processed titanium alloys, the AM titanium alloys usually contain defects such as gas porosity or lack of fusion due to the manufacturing process, and these defects lower the fatigue strength or fatigue life of the AM titanium alloys [36–39]. Hence, it is essential to explore the interior defect induced crack initiation and evolutionary process for VHCF of AM titanium alloys in order to establish precisely the fatigue life prediction model and meet the demand of high safety and reliability of component parts.

Here, we aim to explore the characteristics and mechanism of interior crack initiation and early growth (i.e. the formation of FGA) for VHCF of an AM Ti-6Al-4V alloy. VHCF tests were firstly performed at stress ratios R = -1, 0.1 and 0.2 by ultrasonic frequency fatigue test. Then, the microstructure in FGA under different stress ratios was characterized by scanning electron microscopy (SEM) and electron backscatter diffraction (EBSD). By two-step variable amplitude loadings, we captured the intermediate process of crack initiation and evolution

* Corresponding author.
E-mail addresses: wjwang@bjtu.edu.cn (W. Wang), scq@lnm.imech.ac.cn (C. Sun).

https://doi.org/10.1016/j.ijfatigue.2022.106862
Received 25 October 2021; Received in revised form 12 March 2022; Accepted 14 March 2022
Available online 19 March 2022

through the "tree ring" marks left on the fracture surface. The equivalent crack growth rate in FGA was also measured and used for predicting the fatigue life. Finally, the mechanism of crack initiation and early growth was discussed for the AM Ti-6Al-4V alloy in VHCF regime.

2. Materials and methods

2.1. Materials

The AM Ti-6Al-4V alloy used in this paper was made by the selective laser melting technology on a BLT-S310 machine. At first, the bars with a length of 100 mm and a diameter of 12 mm were produced. Subsequently, they were heat-treated for 2 h at 710 °C in vacuum and then were cooled in argon atmosphere. The building direction was vertical (i.e., 90°). The chemical composition (wt.%) is 5.97 Al, 3.93 V, 0.12 Fe, 0.015 C, 0.088 O, 0.0031 H, and Ti balance for the powder. It was measured by the National Center of Analysis and Testing for Non-ferrous Metals & Electronic Materials in China. The contents of Al, V and Fe were determined by Inductively Coupled Plasma-Atomic Emission Spectrometry (ASTM E2371-13). The content of C was determined by high-frequency combustion-infrared adsorption method (ASTM E1941-2010). The content of O was determined by impulse inert gas fusion-infrared absorption and thermal conductivity method (ASTM E1409-2013). The content of H was determined by impulse inert gas fusion-infrared absorption and thermal conductivity method (ASTM E1447-09 (Reapproved 2016)). The average tensile strength was 1007 MPa, and the average yield strength was 951 MPa. They were obtained from three specimens with a diameter of 5 mm in the gauge section by the Landmark servohydraulic test system (MTS Systems Corporation, USA). The stress versus strain curve is shown in Fig. 1. The testing method followed the National Standard of the People's Republic of China "Metallic materials -Tensile testing at ambient temperature (GB/T 228–2002)".

2.2. Methods

All the fatigue tests were performed in air at room temperature on an ultrasonic fatigue test system USF-2000A (f = 20 kHz) with an adjustable cooling system to reduce the temperature of the specimen during the tests. The fatigue loading without intermittence was applied, as that in Ref. [30]. The stress ratios (R) were −1, 0.1 and 0.2. The sketch map of the specimen tested at R = -1 is shown in Fig. 2a. For the fatigue tests at R = 0.1 and 0.2, both ends of the specimen were connected to the machine with threads, as shown in Fig. 2b.

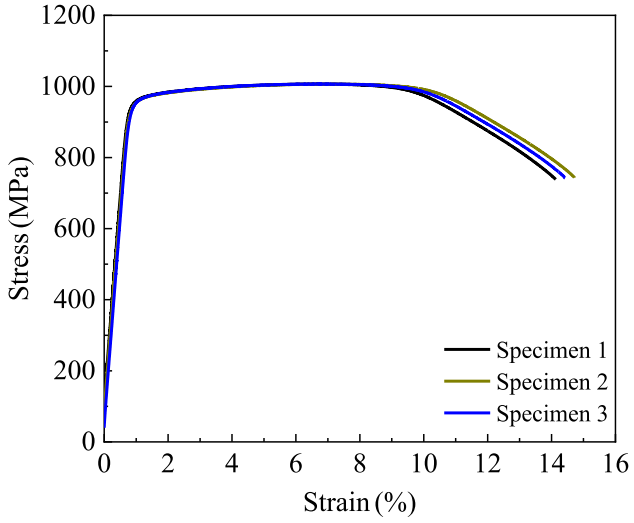

Fig. 1. Stress versus strain curve under tensile test.

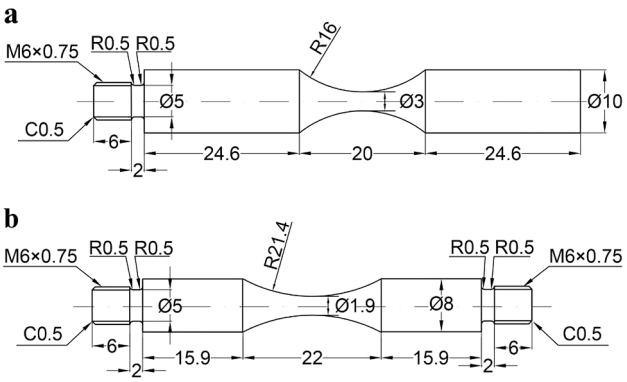

Fig. 2. Shape and geometry of specimens for fatigue tests (in mm). (a) R = -1. (b) R = 0.1 and 0.2.

The constant amplitude fatigue tests were performed at R = -1, 0.1, and 0.2. Based on the results under the constant amplitude loading, the two-step variable amplitude fatigue tests were performed at R = -1. The variable amplitude loadings started from a block of lower stress amplitude $\sigma_{a,L}$ = 400 MPa or 350 MPa with loading cycles $n_L = 3.0 \times 10^6$, 5.0×10^6 or 1.0×10^7, and then was followed by a block of higher stress amplitude $\sigma_{a,H}$ = 625 MPa or 600 MPa with loading cycles $n_H = 4.0 \times 10^3$, except that several specimens experience at first a number of constant amplitude loading σ_a = 350 MPa with 3×10^8 cycles or 2×10^8 cycles. This loading sequence was repeated until the specimen failed. The detailed information for the variable amplitude loadings of specimens is shown in Table 1.

For the constant amplitude loading, the surface temperature of several specimens was measured through a thermocouple (k-type) adhered to the surface of the smallest section of the specimens by the polyimide tape during the ultrasonic frequency fatigue test. Fig. 3 shows the variation of the surface temperature with the loading cycle for the maximum value of the tested stress at different stress ratios. It is seen that, for all the stress ratios R = -1, 0.1 and 0.2, the temperature increases with increasing the loading cycle at the initial loading stage. The temperature stabilizes after about hundreds of thousands of cycles, and the stable temperature is less 50 °C.

After the fatigue test, the fracture surfaces of failed specimens were observed by SEM. For the typical fracture surface morphology, the focused ion beam (FIB) technique was used to extract cross-section samples along the loading direction to further characterize the microstructure in crack initiation and early growth regions at different stress ratios. A coating layer of platinum was used to protect the fracture surface of the extracted samples during the cutting process. The crystallographic information and kernel average misorientation (KAM) analyses were also performed by EBSD and HKL Channel 5™ software in the Oxford Instruments system.

3. Results and discussion

3.1. Microstructure and S-N data

The microstructure of the present AM Ti-6Al-4V alloy is basket-weave. Fig. 4a-4d show the EBSD results of the microstructure near a defect inside the material. The sample was cut along the axis direction of the fatigue specimen, and the observed surface was parallel to the axis direction of the specimen. It is seen that the microstructure of the AM Ti-6Al-4V alloy is inhomogeneous. Some α grains are big, and the grain size is more than 5 μm. Some α grains are small, and the grain size is less than 1 μm, as shown in Fig. 4c and 4d.

S-N data under different stress ratios are shown in Fig. 5. It is seen that the specimens fail in VHCF regime for all the tested stress ratios and the fatigue life increases with decreasing the maximum stress at the

Table 1
Loading information of specimens under variable amplitude loadings.

Specimen No.	$\sigma_{a,L}$ (MPa)	n_L (Cycle)	$\sigma_{a,H}$ (MPa)	n_H (Cycle)	Cumulative cycles at $\sigma_{a,L}$	Cumulative cycles at $\sigma_{a,H}$
1	400	3.0×10^6	625	4.0×10^3	3.0×10^7	4.0×10^4
2	400	3.0×10^6	625	4.0×10^3	2.2×10^8	2.9×10^5
3	400	3.0×10^6	600	4.0×10^3	5.4×10^7	6.9×10^4
4	400	3.0×10^6	600	4.0×10^3	1.6×10^8	2.1×10^5
5	400	3.0×10^6	600	4.0×10^3	2.4×10^7	3.2×10^4
6	400	3.0×10^6	600	4.0×10^3	1.5×10^7	2.0×10^4
7*	350	5.0×10^6	600	4.0×10^3	3.4×10^8	2.8×10^3
8*	350	5.0×10^6	600	4.0×10^3	3.5×10^8	4.0×10^3
9*	350	5.0×10^6	600	4.0×10^3	7.3×10^8	3.4×10^5
10*	350	5.0×10^6	600	4.0×10^3	3.1×10^8	8.0×10^3
11*	350	1.0×10^7	625	4.0×10^3	6.3×10^8	1.7×10^5

* It experiences at first a number of constant amplitude loading σ_a = 350 MPa with 3×10^8 cycles for specimens 7 to 10 and 2×10^8 cycles for specimen 11, respectively.

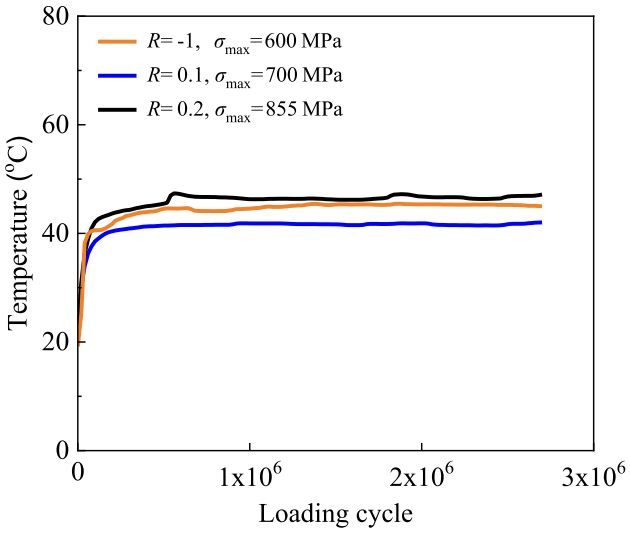

Fig. 3. Variation of surface temperature of specimens with loading cycle during ultrasonic frequency fatigue test.

same stress ratio.

3.2. Microstructure characteristic in FGA

Under constant amplitude loading, the fatigue cracks of failed specimens at R = -1, 0.1 and 0.2 all initiate from the internal defects, such as hole or lack of fusion, and the crack initiation and early growth region exhibits FGA feature, as shown in Fig. 6a–6c. The multiple internal crack initiations with FGA feature are also observed at the fracture surface (Fig. 6c and 6d), which shows the evidence of the competition of internal crack initiation induced by defects. For a further characterization of the microstructure in FGA, four cross-sectional samples along the loading direction were extracted for the specimens tested at different stress ratios by FIB technique. Samples 1 and 2 were extracted from a specimen tested at R = -1, as shown in Fig. 6a. Sample 1 was next to the defect, and sample 2 was a little far from the defect. Samples 3 and 4 were extracted from the specimens tested at positive stress ratios, as shown in Fig. 6b and 6d, respectively. Sample 3 was extracted from a specimen tested at R = 0.1, and sample 4 was located at a secondary crack initiation region with FGA feature of a specimen tested at R = 0.2. The EBSD results are shown in Fig. 6e–6h, respectively. It is seen from Fig. 6e–6h that there are nano-sized irregular α grains with low angle grain boundaries (LAGBs) or high angle grain boundaries (HAGBs) in some local regions near the fracture surface in FGA. The feature of local nanograin regions in FGA is irrespective of stress ratios (negative stress ratio or positive stress ratio) and the location from the crack origin (defect). This phenomenon differs from the existing observations for the AM Ti-6Al-4V alloy failed from the internal defect with FGA feature, in which a layer of nanograins exist along the fracture surface at R = -1, and no nanograins are found at positive stress ratios [26].

EBSD results of the microstructure in FGA indicate that the nanograins should be an important factor for the interior crack initiation and evolution of the AM Ti-6Al-4V alloy in VHCF regime. Herein, the nano-sized α grains with HAGBs near the fracture surface in FGA (Fig. 6e–6h) are measured and analyzed, which is also compared with the original tiny α grains (i.e. the α grains in the rectangular areas in Fig. 4c) of the material that do not suffer from fatigue loadings. The distribution of the grain size is shown in Fig. 7. It is observed that the tiny α grains in the local regions are all with HAGBs for the original material. While for the nanograins near the fracture surface in FGA, both LAGBs and HAGBs are found at negative and positive stress ratios. Moreover, it is seen from Fig. 7 that the nanograins with HAGBs are less than 280 nm in size in FGA, which are appreciably below the smallest grain size of the tiny α grains in the original material. This result indicates that the nanograins in FGA are formed during the fatigue tests rather than the original tiny α grains. It is also supported by the KAM map for the extracted samples in Fig. 6e–6h that the strain localization or plastic deformation is more significant for the refined grain regions.

3.3. Crack growth and evolution in FGA

By employing two-step variable amplitude loadings, some specimens exhibit "tree ring" like patterns on the fracture surface, as shown in Fig. 8. Considering that the FGA size tends to be larger with a decrease of stress amplitude under constant amplitude loading (Fig. 9) and that the higher stress generally leads to a bigger crack growth rate than the lower stress, the fine granular area feature in Fig. 8e–8 h is due to the block of the lower stress, and the relative smooth area between the fine granular areas is the result of the block of the higher stress. The "tree ring" marks (i.e. difference of morphology characteristic) left on the fracture surface provide the information for the intermediate process of the crack growth and evolution in FGA, and make it possible to estimate the equivalent crack growth rate in FGA. Here, the fatigue cracks after and before the block of the lower stress are approximately seen as concentric mode-I internal penny cracks in an infinite solid under a uniform remote tensile stress σ, and the radii in the direction of the crack extension with relative clear marks are considered [10,29], as shown in Fig. 8e–8 h. The stress intensity factor range ΔK and the associated (equivalent) crack growth rate da/dN are calculated by $\Delta\sigma_{a,H}\sqrt{2(r_i + r_{i+1})/\pi}$ and $(r_{i+1} - r_i)/n_H$ for the higher stress (i = 1, 3, 5), and $\Delta\sigma_{a,L}\sqrt{2(r_{i+1} + r_{i+2})/\pi}$ and $(r_{i+2} - r_{i+1})/n_L$ for the lower stress (i = 1, 3), respectively, where r_1, r_3, r_5 denote the radii of penny cracks after the block of the lower stress, and r_2, r_4, r_6 denote the radii after the block of the higher stress. The values of the measured radii for the penny cracks are listed in Table 2.

Fig. 10a shows the variation of the crack growth rate with the value

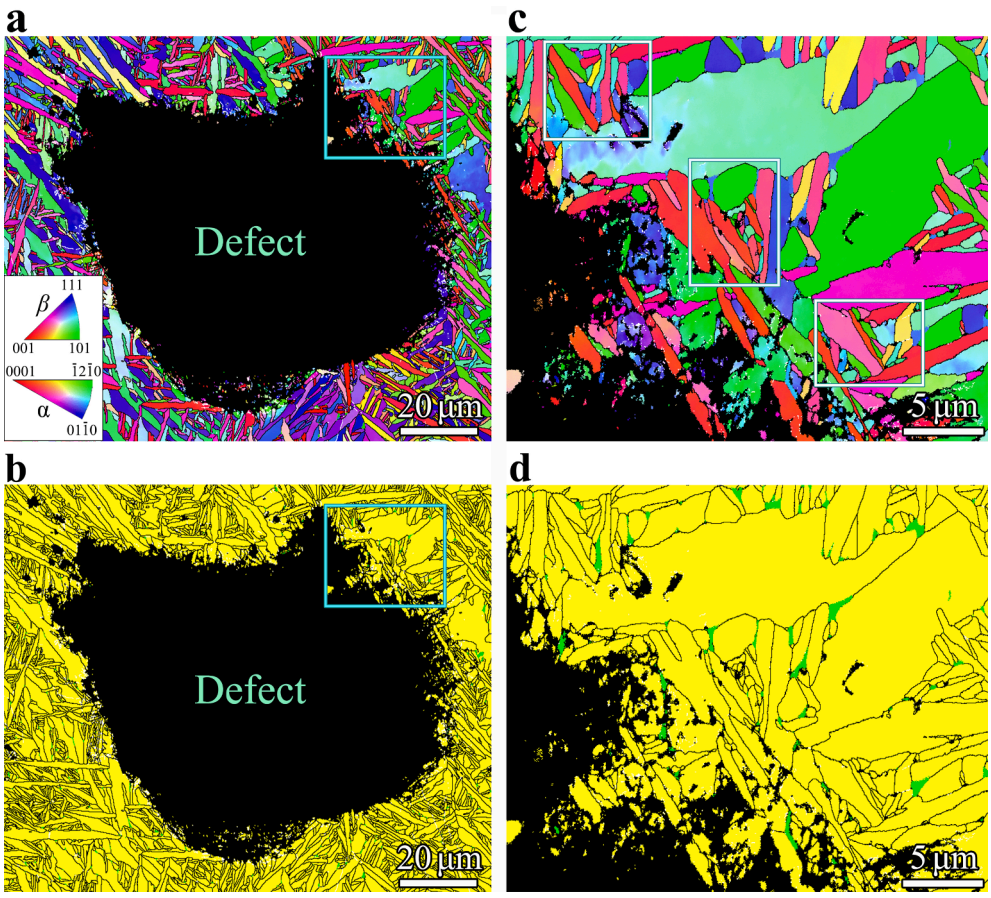

Fig. 4. EBSD results of the microstructure near a defect inside the material. (a) Inverse pole figure (IPF). (b) Phase map. (c) and (d) Enlarged images in the rectangular area in (a) and (b), respectively. The rectangular areas in (c) are used for the statistics of α grain size.

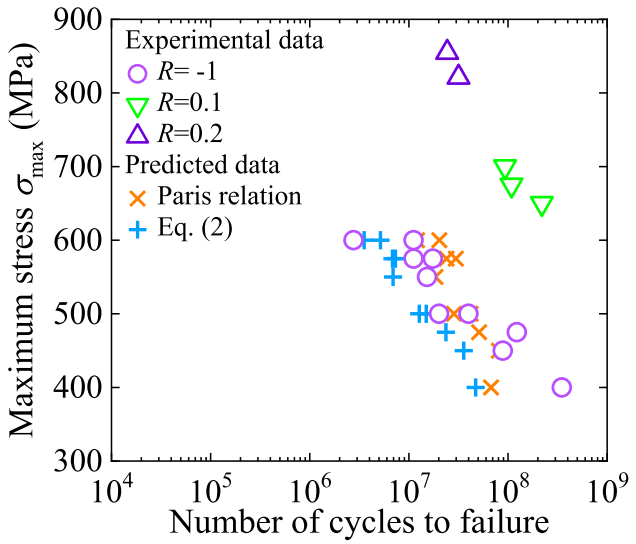

Fig. 5. S–N data at different stress ratios, in which the symbol "cross" and "plus" denote the predicted fatigue life at R = -1 by Paris relation and the model Eq. (2), respectively.

of ΔK for both the block of the higher stress and the lower stress. The result is also compared with those of the wrought Ti-6Al-4V alloy under ultrasonic frequency fatigue test at $R = -1$ in air [40] and the AM Ti-6Al-4V alloy with stress-relief heat treatment (the crack propagation direction parallels to the building layers) at $R = 0.1$ in air [41] by the consideration that no result is available for the near-threshold crack growth rate of the AM Ti-6Al-4V alloy at $R = -1$ as far as the authors' knowledge. It is seen from Fig. 10a that the equivalent crack growth rate in FGA is very slow (much lower than one lattice spacing per cycle) in comparison with the crack growth rate (bigger than 10^{-10} m/cyc) associated with the block of the higher stress. The ultralow crack growth rate in FGA indicates that the crack does not grow in all directions at each loading cycle in the crack initiation and early growth stage of VHCF, which extends at first in some local regions after a number of cycles due to the microstructure inhomogeneity. This result is consistent with the SEM observation in Fig. 8h for the crack initiation and evolution captured in FGA under variable amplitude loadings. For the same block of the lower stress amplitude, the expansion of the fine granular area has a discrepancy in different directions from the crack origin.

For the comparison of the present interior crack growth rate with that of the AM Ti-6Al-4V alloy at $R = 0.1$ in air [41], the frequency is assumed to have no significant effect on the near-threshold fatigue crack growth rate [42]. The effect of R on the near-threshold crack growth rate and the crack growth rate on Paris region of metallic materials can be described by the cracking driving parameter $f(R)\Delta K$ with $f(R) = (1–R)^{-\alpha}$, or $f(R) = (1–R)^{-\alpha}$ for $R \geq 0$ and $(1–R)^{-1}$ for $R < 0$ [43,44], namely that the variation of the crack growth rate with the stress intensity factor range has a similar trend at different stress ratios. Consequently, the results in Fig. 10a indicate that the crack growth rate (lower than 10^{-10} m/cyc) for the interior defect induced cracking of the AM Ti-6Al-4V alloy increases much lower than that in air with the increase of the stress intensity factor range. A similar result is also indicated for the comparison of the interior crack growth rate (lower than 10^{-10} m/cyc) of the present AM Ti-6Al-4V alloy with the crack growth rate of the wrought Ti-6Al-4V alloy in air [40], as shown in Fig. 10a.

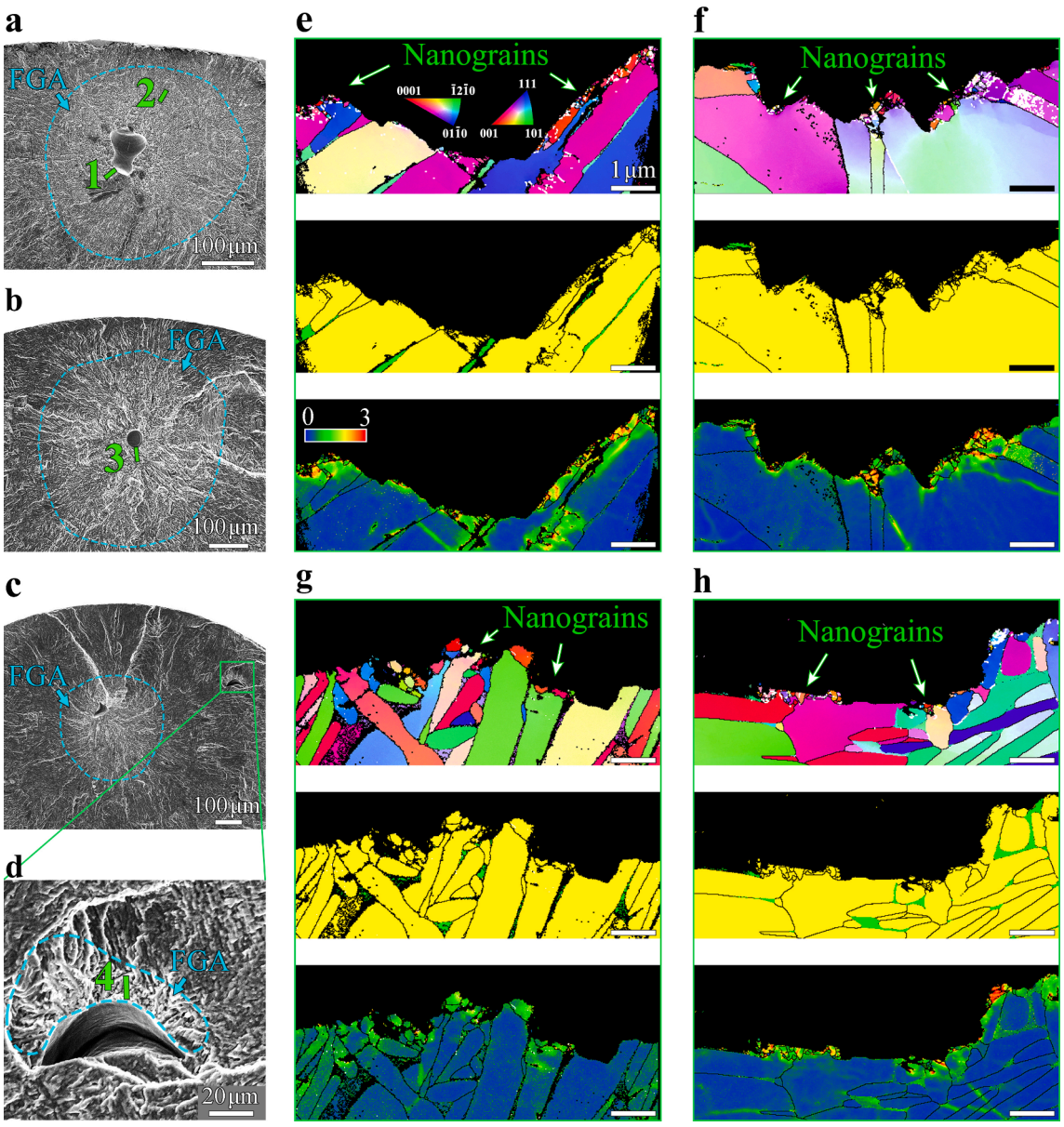

Fig. 6. Fracture surface morphology and microstructure characteristic in FGA. (a)–(c) SEM observation of fracture surfaces at $R = -1$ ($\sigma_{max} = 400$ MPa and $N_f = 3.5 \times 10^8$ cyc), $R = 0.1$ ($\sigma_{max} = 650$ MPa and $N_f = 2.2 \times 10^8$ cyc) and $R = 0.2$ ($\sigma_{max} = 821$ MPa and $N_f = 3.2 \times 10^7$ cyc), respectively, in which the short lines denote the locations where the cross-sectional samples are extracted. (d) Enlarged images of the secondary crack in (c). (e)–(h) EBSD results of the cross-sectional samples 1–4 shown in (a)–(d), respectively, in which the top panel is IPF, the middle panel is phase map and the bottom panel is KAM map. The black line denotes the HAGBs (greater than 10°) and the white line denotes the LAGBs (2°~10°) in IPF in (e)–(h). All scale bars in (e)–(h) are 1 μm.

3.4. Mechanism of FGA formation

The present results show that the FGA morphology is a typical feature for the interior defect induced failure in VHCF regime, and the microstructure in FGA exhibits discontinuous regions of nanograins. One point of view is that FGA is formed by the repeated contact of fracture surface after the crack formation [28,32,33]. This viewpoint cannot explain well the case that the FGA feature with discontinuous regions of nanograins is observed at positive stress ratios $R = 0.1$ and 0.2 (Fig. 6). This indicates that the nanograins are formed before the fatigue crack formation. The ultralow crack growth rate (lower than one lattice spacing per cycle) in FGA provides the possibility that the dislocation interaction or plastic deformation in the local highly stressed region (e.g. the crack origin and the crack tip) leads to the occurrence of grain refinement. The microstructure evolution through dislocation rearrangement then leading to the formation of small sub-grains or LAGBs has been observed for VHCF of a medium carbon steel [48]. The nanograins with both LAGBs and HAGBs observed in the α grains near the fracture surface in FGA further indicate that the grain refinement is related to the dislocation interaction or plastic deformation [10,24,29,30,34,35]. During the following cyclic loadings, the cracks form along the nanograin-common grain interface or within the nanograins due to the decrease of threshold value for crack initiation in the refined grain regions [24][49]. The crack formation in these two cases has been observed in VHCF of high strength steels [11,25]. On the other hand, due to the deformation incompatibility or microstructure inhomogeneity, the fatigue crack of the AM Ti-6Al-4V alloy could form at defects, interfaces, larger α-phase, etc. [17,18,30,50]. In this case, the fatigue crack forms irrespective of the grain refinement.

Therefore, the FGA formation for the AM Ti-6Al-4V alloy in VHCF regime is the result of the fatigue crack induced by the refined grains in combination with the crack formation irrespective of the grain

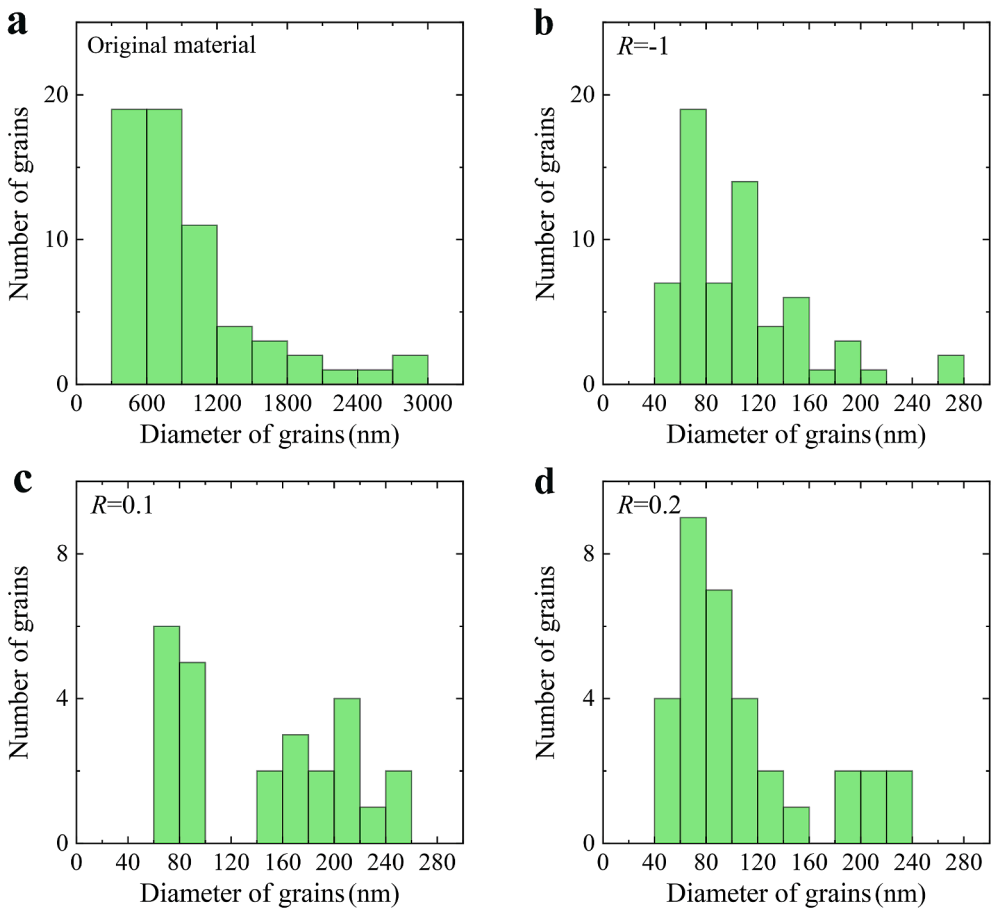

Fig. 7. Distribution of grain size. (a) Tiny α grains in local regions of original material. (b)–(d) Nano-sized α grains with HAGBs near the crack surface of the samples in Fig. 6e and 6f, Fig. 6g and Fig. 6h, respectively.

refinement [30]. The sketch map of the FGA formation (i.e. the mechanism of crack initiation and early growth) induced by interior defect is illustrated in Fig. 11.

Stage I: The local high stress caused by the defect induces the formation of dislocation or dislocation cells in local regions or the nuclei of micro-cracks near the defect.

Stage II: Nanograins with LAGBs or HAGBs form in the local regions during further cyclic loadings, and the micro-cracks form within nanograins or along nanograin-common grain interface. During this process, the micro-cracks might also form at the larger α-phase or the interface of coarse grains, etc., due to deformation incompatibility or microstructure inhomogeneity.

Stage III: The micro-cracks coalesce, and some new micro-cracks form due to grain refinement or irrespective of grain refinement. The main crack extends, and the growing crack causes the grain refinement or micro-crack formation again.

Stage IV: Stage III continues under the further fatigue loading until the FGA forms.

It is noted that the fatigue crack could also initiate at grains, interfaces, etc. The sketch map in Fig. 11 only presents the case of interior defect induced crack initiation with FGA morphology and discontinuous regions of nanograins for the AM Ti-6Al-4V alloy. The model explains the phenomenon that the microstructure in FGA exhibits a layer of nanograins for the AM Ti-6Al-4V alloy and the conventionally processed Ti-6Al-4V in VHCF regime [23,26], which is a special case of the proposed mechanism that FGA formation is due to the grain refinement followed by cracks.

3.5. Crack growth rate model and fatigue life prediction

According to the results for high strength steels with FGA feature in the crack initiation and early growth region [45,46], the equivalent crack growth rate in FGA is related to the initiated crack size, the stress amplitude σ_a and the yield strength σ_Y of the material. When the initiated crack is taken as a penny crack, the equivalent crack growth rate in FGA is written as [46]

$$\frac{da}{dN} = \alpha\left(\frac{\sigma_a}{\sigma_Y}\right)^l a \tag{1}$$

in which a denotes the radius of the penny crack, i.e. $a = \sqrt{area_r/\pi}$, $area_r$ is the area of the initiated crack region, α and l are parameters.

The fatigue life consumed in FGA is expressed as

$$N_f = \frac{1}{\alpha}\left(\frac{\sigma_a}{\sigma_Y}\right)^{-l} \ln\frac{a_{FGA}}{a_0} \tag{2}$$

where $a_{FGA} = \sqrt{area_{FGA}/\pi}$ and $a_0 = \sqrt{area_{def}/\pi}$, $area_{FGA}$ and $area_{def}$ denote FGA area and defect area on the crack surface, respectively.

Considering that the equivalent crack growth rate in FGA has the tendency to increase with increasing the value of ΔK, the Paris equation [47] is also used to fit the equivalent crack growth rate in FGA and to predict the fatigue life, i.e.

$$\frac{da}{dN} = C(\Delta K)^m \tag{3}$$

in which the interior crack is also seen as a penny crack with the area $area_r$, a is the radius of the penny crack, ΔK is the stress intensity factor range for the interior crack, i.e. $\Delta K = 4\sigma_a\sqrt{a/\pi}$, C and m are parameters.

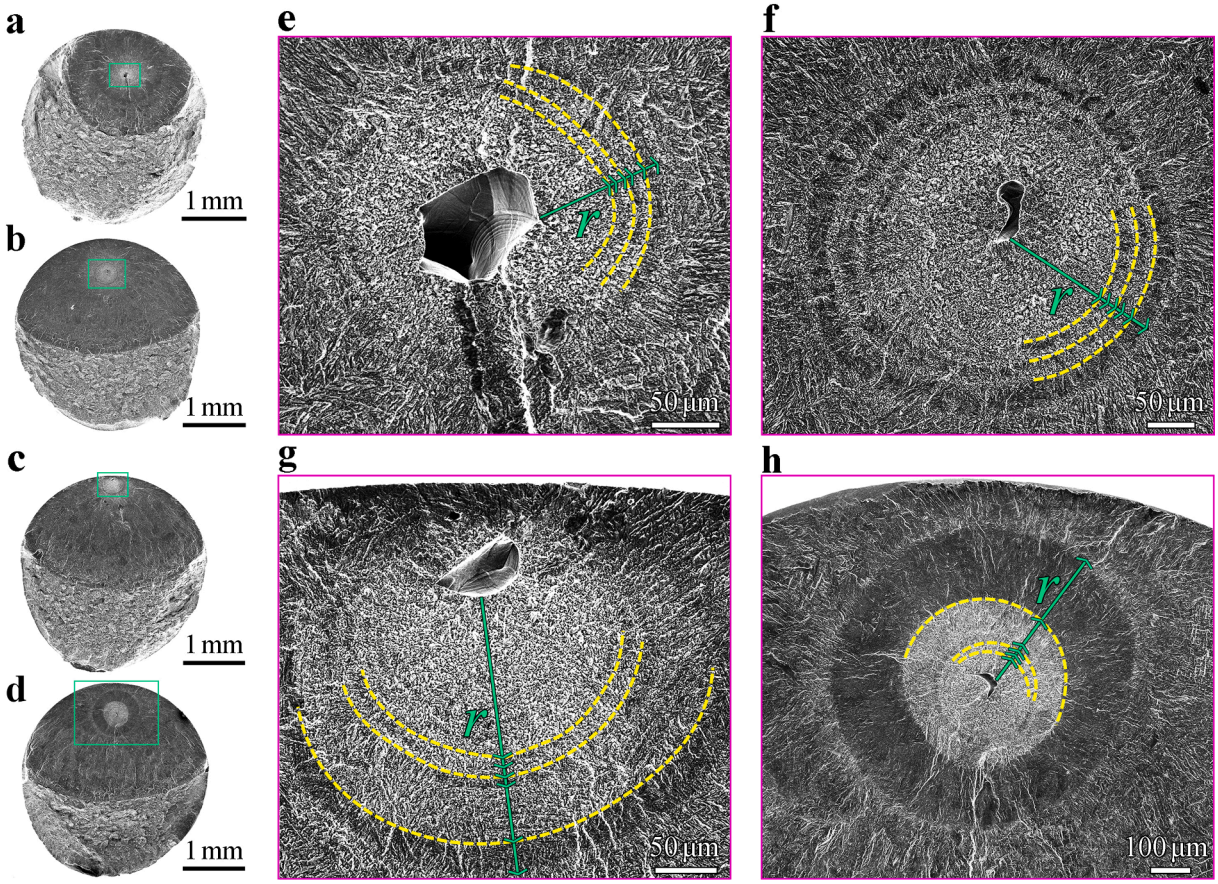

Fig. 8. Tree ring like pattern on fracture surface under variable amplitude loadings. (a) and (e) Specimen 3. (b) and (f) Specimen 4. (c) and (g) Specimen 9. (d) and (h) Specimen 11. The dashed lines denote the marks where a block of the lower stress is changed to a block of the higher stress, and the arrows denote the radii of approximately concentric penny cracks for measurement.

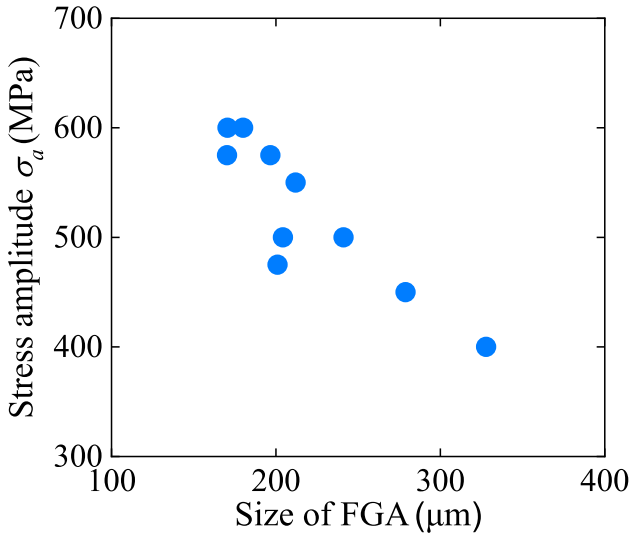

Fig. 9. FGA size versus stress amplitude at R = -1 under constant amplitude loading.

From Eq. (3), the fatigue life consumed in FGA is

$$N_f = \frac{2\pi^{\frac{m}{2}}}{C(2-m)(4\sigma_a)^m}[(a_{\mathrm{FGA}})^{1-\frac{m}{2}} - (a_0)^{1-\frac{m}{2}}] \quad (4)$$

The model results for the equivalent crack growth rate in FGA by Eqs. (1) and (3) are shown in Fig. 10b. The parameters are obtained by fitting all the experimental data in Fig. 10b. It seems that the crack growth rate models Eqs. (1) and (3) both show a good agreement with the experimental data. The difference is that the equivalent crack growth rate described by Eq. (1) increases lower than that described by the Paris relation.

Table 2
Values of measured radii for penny cracks shown in Fig. 8.

Specimen No.	3	4	9	11
r_1 (μm)	55.3	129.9	110.1	67.9
r_2 (μm)	60.9	134.6	120.1	78.4
r_3 (μm)	67.1	142.9	127.4	91.9
r_4 (μm)	73.6	152.3	137.9	109.2
r_5 (μm)	82.4	195.0	147.1	184.6
r_6 (μm)	93.5	222.8	169.6	360.8

For a further comparison, these two crack growth rate models are used to predict the fatigue life at R = -1 under constant amplitude loading. The predicted results are shown in Fig. 5. Here, the difference of the lifetime consumed in FGA and the total fatigue life is not considered for the comparison in Fig. 5 due to that FGA consumes most of the fatigue life in VHCF regime [8–10,22,23]. It is seen that the predicted fatigue lifetimes are close to the experimental results for both the crack growth rate models. The crack growth rate model Eq. (1) gives conservative fatigue life prediction in VHCF regime. While the predicted fatigue life by the crack growth rate model Eq. (4) is higher for the specimens with fatigue life between 1×10^7 and 2×10^7 cycles, and is lower for the specimens with fatigue life larger than 10^8 cycles. Considering that the equivalent crack growth rate in FGA is measured along the direction of crack extension with relative clear marks in Sec.

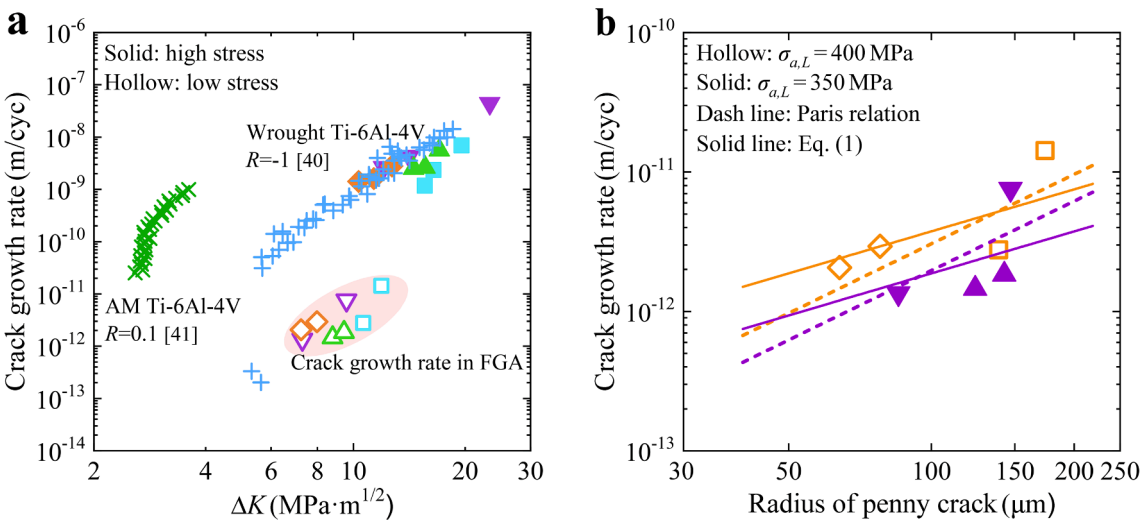

Fig. 10. Comparison of crack growth rate and crack growth rate model. (a) Comparison of the present crack growth rate with the data in Refs. [40,41]. (b) Comparison of crack growth rate models.

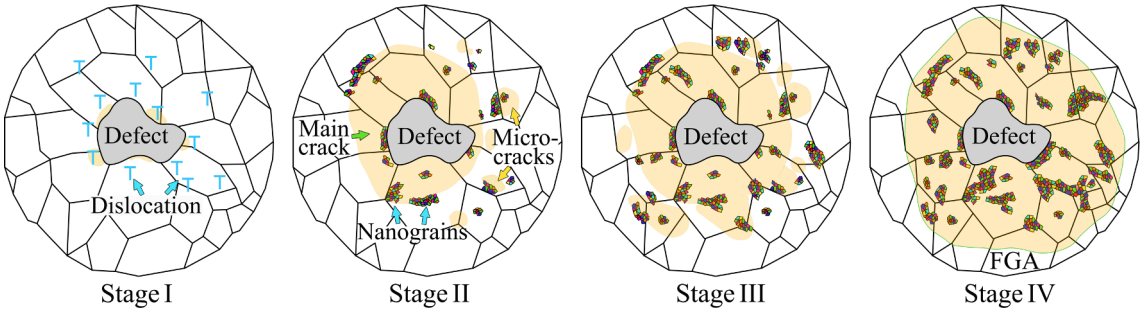

Fig. 11. Schematic of FGA formation at interior defect. Faint yellow color: crack initiation and early growth region.

3.3, the crack growth rate described by Eqs. (1) and (3) are higher than the actual equivalent crack growth rate in FGA. Consequently, the predicted fatigue life by Eqs. (2) and (4) should be lower than the experimental one in Fig. 5. From this view, the crack growth rate model Eq. (1) is better for describing the crack growth behavior in FGA and estimating the fatigue life for the interior defect induced failure in VHCF regime.

By employing Eq. (1), the equivalent crack growth rate near the defect can be extrapolated for the interior defect deduced failure. Here, we use the lowest stress amplitude σ_a = 350 MPa under variable amplitude loadings and the defect sizes at R = -1 under constant amplitude loading for analysis. The values of the defect radius are between 19 μm and 41 μm. From Eq. (1), the equivalent crack growth rate near the defect is between 3.56×10^{-13} m/cyc and 7.68×10^{-13} m/cyc. This indicates that the equivalent crack growth rate in FGA could be in the magnitude of 10^{-13} m/cyc for the present loading condition of the AM Ti-6Al-4V alloy.

4. Conclusions

In this paper, the interior crack initiation and early growth is investigated for an AM Ti-6Al-4V alloy by selective laser melting technology. The findings provide an insight into the process of the interior crack initiation and microstructure evolution for Ti-alloys in VHCF regime. The main results are as follows.

(1) The interior crack initiation and early growth region exhibits FGA morphology and the microstructure in FGA presents discontinuous regions of nanograins in VHCF regime. The "tree ring" marks left on the fracture surface by variable amplitude loadings indicate that the crack growth in FGA accelerates gradually with increasing the loading cycle and the equivalent crack growth rate in FGA is lower than one lattice spacing (~10^{-10} m) per cycle.

(2) The equivalent crack growth rate in FGA could be modelled as $da/dN = \alpha(\sigma_a/\sigma_Y)^l a$, where $a = \sqrt{area_r/\pi}$, $area_r$ is the area of the initiated crack region, α and l are parameters. The predicted fatigue life accords with the experimental data under the constant amplitude loading. The crack growth rate (lower than 10^{-10} m/cyc) for the interior defect induced cracking increases much lower than that of the wrought Ti-6Al-4V alloy and the AM Ti-6Al-4V alloy in air with increasing the stress intensity factor range.

(3) The nanograins formed during the fatigue process play an important role in the interior crack initiation and evolution of Ti-alloys in VHCF regime. The mechanism of interior defect induced crack initiation and early growth (i.e. FGA) of AM Ti-6Al-4V alloys is attributed to the formation of nanograins caused by dislocation interaction over a number of cyclic loadings followed by cracks in combination with the cracks formed at defects, α-phase, interfaces, etc. during cyclic loadings. The model for FGA formation shows a good explanation for the observation of the microstructure in FGA whether it is a layer of nanograins or it exhibits discontinuous regions of nanograins.

Declaration of Competing Interest

The authors declare that they have no known competing financial interests or personal relationships that could have appeared to influence the work reported in this paper.

Acknowledgements

The authors acknowledge the support of the National Natural Science Foundation of China Basic Science Center for "Multiscale Problems in Nonlinear Mechanics" (11988102), the National Natural Science Foundation of China (91860112) and the Science and Technology Research and Development Program of China State Railway Group Co., Ltd. (P2020J024).

References

[1] Herzog D, Seyda V, Wycisk E, Emmelmann C. Additive manufacturing of metals. Acta Mater 2016;117:371–92.
[2] Liu G, Zhang X, Chen X, He Y, Cheng L, Huo M, et al. Additive manufacturing of structural materials. Mater Sci Eng R Reports 2021;145:100596.
[3] Nouri A, Rohani Shirvan A, Li Y, Wen C. Additive manufacturing of metallic and polymeric load-bearing biomaterials using laser powder bed fusion: A review. J Mater Sci Technol 2021;94:196–215.
[4] Murr LE, Quinones SA, Gaytan SM, Lopez MI, Rodela A, Martinez EY, et al. Microstructure and mechanical behavior of Ti–6Al–4V produced by rapid-layer manufacturing, for biomedical applications. J Mech Behav Biomed Mater 2009;2(1):20–32.
[5] Jiao S, Gao C, Cheng Li, Li X, Feng Yu. A very high-cycle fatigue test and fatigue properties of TC17 titanium alloy. J Mater Eng Perform 2016;25(3):1085–93.
[6] Li Y, Song Q, Feng S, Sun C. Effects of loading frequency and specimen geometry on high cycle and very high cycle fatigue life of a high strength titanium alloy. Materials (Basel) 2018;11:1628.
[7] Huang ZY, Liu HQ, Wang C, Wang QY. Fatigue life dispersion and thermal dissipation investigations for titanium alloy TC17 in very high cycle regime. Fatigue Fract Eng Mater Struct 2015;38:1285–93.
[8] Murakami Y, Nomoto T, Ueda T, Murakami Y. On the mechanism of fatigue failure in the superlong life regime ($N>10^7$ cycles). Part 1: influence of hydrogen trapped by inclusions. Fatigue Fract Eng Mater Struct 2000;23:893–902.
[9] Shiozawa K, Morii Y, Nishino S, Lu L. Subsurface crack initiation and propagation mechanism in high-strength steel in a very high cycle fatigue regime. Int J. Fatigue 2006;28(11):1521–32.
[10] Sun C, Song Q, Zhou L, Pan X. Characteristic of interior crack initiation and early growth for high cycle and very high cycle fatigue of a martensitic stainless steel. Mater Sci Eng A 2019;758:112–20.
[11] Sun C, Song Q, Zhou L, Liu J, Wang Y, Wu X, et al. The formation of discontinuous gradient regimes during crack initiation in high strength steels under very high cycle fatigue. Int J Fatigue 2019;124:483–92.
[12] Torabian N, Favier V, Dirrenberger J, Adamski F, Ziaei-Rad S, Ranc N. Correlation of the high and very high cycle fatigue response of ferrite based steels with strain rate-temperature conditions. Acta Mater 2017;134:40–52.
[13] Wang QY, Lib T, Zenga XG. Gigacycle fatigue behavior of high strength aluminum alloys. Procedia Eng 2010;2(1):65–70.
[14] Nie B, Zhang Z, Zhao Z, Zhong Q. Effect of anodizing treatment on the very high cycle fatigue behavior of 2A12-T4 aluminum alloy. Mater Des 2013;50:1005–10.
[15] Takahashi Y, Shikama T, Yoshihara S, Aiura T, Noguchi H. Study on dominant mechanism of high-cycle fatigue life in 6061–T6 aluminum alloy through microanalyses of microstructurally small cracks. Acta Mater 2012;60:2554–67.
[16] Cervellon A, Hémery S, Kürnsteiner P, Gault B, Kontis P, Cormier J. Crack initiation mechanisms during very high cycle fatigue of Ni-based single crystal superalloys at high temperature. Acta Mater 2020;188:131–44.
[17] Günther J, Krewerth D, Lippmann T, Leuders S, Tröster T, Weidner A, et al. Fatigue life of additively manufactured Ti-6Al-4V in the very high cycle fatigue regime. Int J Fatigue 2017;94:236–45.
[18] Qian G, Li Y, Paolino DS, Tridello A, Berto F, Hong Y. Very-high-cycle fatigue behavior of Ti-6Al-4V manufactured by selective laser melting: Effect of build orientation. Int J Fatigue 2020;136:105628.
[19] Tridello A, Fiocchi J, Biffi CA, Chiandussi G, Rossetto M, Tuissi A, et al. VHCF response of heat-treated SLM Ti6Al4V Gaussian specimens with large loaded volume. Procedia Struct Integr 2019;18:314–21.
[20] Murakam Y, Nomoto T, Ueda T. Factors influencing the mechanism of superlong fatigue failure in steels. Fatigue Fract Eng Mater Struct 1999;22(7):581–90.
[21] Shiozawa K, Lu L, Ishihara S. S-N curve characteristics and subsurface crack initiation behaviour in ultra-long life fatigue of a high carbon-chromium bearing steel. Fatigue Fract Eng Mater Struct 2001;24(12):781–90.
[22] Hong Y, Lei Z, Sun C, Zhao A. Propensities of crack interior initiation and early growth for very-high-cycle fatigue of high strength steels. Int J Fatigue 2014;58:144–51.
[23] Su H, Liu X, Sun C, Hong Y. Nanograin layer formation at crack initiation region for very-high-cycle fatigue of a Ti–6Al–4V alloy. Fatigue Fract Eng Mater Struct 2017;40(6):979–93.
[24] Grad P, Reuscher B, Brodyanski A, Kopnarski M, Kerscher E. Mechanism of fatigue crack initiation and propagation in the very high cycle fatigue regime of high-strength steels. Scr Mater 2012;67(10):838–41.
[25] Tofique MW, Bergström J, Svensson K. Very high cycle fatigue of cold rolled stainless steels, crack initiation and formation of the fine granular area. Int J Fatigue 2017;100:238–50.
[26] Du L, Pan X, Qian G, Zheng L, Hong Y. Crack initiation mechanisms under two stress ratios up to very-high-cycle fatigue regime for a selective laser melted Ti-6Al-4V. Int J Fatigue 2021;149:106294.
[27] Sakai T, Oguma N, Morikawa A. Microscopic and nanoscopic observations of metallurgical structures around inclusions at interior crack initiation site for a bearing steel in very high-cycle fatigue. Fatigue Fract Eng Mater Struct 2015;38:1305–14.
[28] Hong Y, Liu X, Lei Z, Sun C. The formation mechanism of characteristic region at crack initiation for very-high-cycle fatigue of high-strength steels. Int J Fatigue 2016;89:108–18.
[29] Song Q, Sun C. Mechanism of crack initiation and early growth of high strength steels in very high cycle fatigue regime. Mater Sci Eng A 2020;771:138648.
[30] Sun C, Chi W, Wang W, Duan Y. Characteristic and mechanism of crack initiation and early growth of an additively manufactured Ti-6Al-4V in very high cycle fatigue regime. Int J Mech Sci 2021;205:106591.
[31] Zhu M-L, Jin L, Xuan F-Z. Fatigue life and mechanistic modeling of interior micro-defect induced cracking in high cycle and very high cycle regimes. Acta Mater 2018;157:259–75.
[32] Nakamura T, Oguma H, Shinohara Y. The effect of vacuum-like environment inside sub-surface fatigue crack on the formation of ODA fracture surface in high strength steel. Procedia Eng 2010;2(1):2121–9.
[33] Ogawa T, Stanzl-Tschegg SE, Schönbauer BM. A fracture mechanics approach to interior fatigue crack growth in the very high cycle regime. Eng Fract Mech 2014;115:241–54.
[34] Wang C, Liu Y, Nikitin A, Wang Q, Zhou M. A general scenario of fish-eye crack initiation on the life of high-strength steels in the very high-cycle fatigue regime. Fatigue Fract Eng Mater Struct 2019;42(9):2183–94.
[35] Zhang H, Yu F, Li S, He E. Fine granular area formation by damage-induced shear strain localization in very-high-cycle fatigue. Fatigue Fract Eng Mater Struct 2021;44:2489–502.
[36] Edwards P, Ramulu M. Fatigue performance evaluation of selective laser melted Ti-6Al-4V. Mater Sci Eng A 2014;598:327–37.
[37] Masuo H, Tanaka Y, Morokoshi S, Yagura H, Uchida T, Yamamoto Y, et al. Effects of defects, surface roughness and HIP on fatigue strength of Ti-6Al-4V manufactured by additive manufacturing. Procedia Struct Integr 2017;7:19–26.
[38] Greitemeier D, Palm F, Syassen F, Melz T. Fatigue performance of additive manufactured TiAl6V4 using electron and laser beam melting. Int J Fatigue 2017;94:211–7.
[39] Tammas-Williams S, Withers PJ, Todd I, Prangnell PB. The influence of porosity on fatigue crack initiation in additively manufactured titanium components. Sci Rep 2017;7:7308.
[40] Stanzltschegg S. Fatigue crack growth and thresholds at ultrasonic frequencies. Int J Fatigue 2006;28(11):1456–64.
[41] Becker TH, Dhansay NM, Haar GMT, Vanmeensel K. Near-threshold fatigue crack growth rates of laser powder bed fusion produced Ti-6Al-4V. Acta Mater 2020;197:269–82.
[42] Boyce BL, Ritchie RO. Effect of load ratio and maximum stress intensity on the fatigue threshold in Ti–6Al–4V. Eng Fract Mech 2001;68(2):129–47.
[43] Dinda S, Kujawski D. Correlation and prediction of fatigue crack growth for different R-ratios using Kmax and ΔK^+ parameters. Eng Fract Mech 2004;71(12):1779–90.
[44] Sun C, Lei Z, Hong Y. Effects of stress ratio on crack growth rate and fatigue strength for high cycle and very-high-cycle fatigue of metallic materials. Mech Mater 2014;69(1):227–36.
[45] Sun C, Xie J, Zhao A, Lei Z, Hong Y. A cumulative damage model for fatigue life estimation of high-strength steels in high-cycle and very-high-cycle fatigue regimes. Fatigue Fract Eng Mater Struct 2012;35(7):638–47.
[46] Sun C, Liu X, Hong Y. A two-parameter model to predict fatigue life of high-strength steels in a very high cycle fatigue regime. Acta Mech Sin 2015;31(3):383–91.
[47] Paris PC, Erdogan F. A critical analysis of crack propagation laws. J Basic Eng 1963;85:528–34.
[48] Koster M, Wagner G, Eifler D. Cyclic deformation behavior of a medium carbon steel in the VHCF regime. Procedia Eng 2010;2(1):2189–97.
[49] Niendorf T, Rubitschek F, Maier HJ, Canadinc D, Karaman I. On the fatigue crack growth–microstructure relationship in ultrafine-grained interstitial-free steel. J Mater 2010;45(17):4813–21.
[50] Zuo JH, Wang ZG, Han EH. Effect of microstructure on ultra-high cycle fatigue behavior of Ti-6Al-4V. Mater Sci Eng. a-Structural Mater. Prop Microstruct Process 2008;473(1-2):147–52.